



UNIVERSITY OF LEEDS

This is a repository copy of *A novel Z-scheme SnS/NiAl-LDH/g-C<sub>3</sub>N<sub>4</sub> heterojunction for piezo-photocatalytic degradation of tetracycline: Performance and mechanism.*

White Rose Research Online URL for this paper:

<https://eprints.whiterose.ac.uk/id/eprint/215544/>

Version: Accepted Version

---

**Article:**

Sun, H., Tillotson, M.R. [orcid.org/0000-0002-3362-021X](https://orcid.org/0000-0002-3362-021X), Wang, D. et al. (1 more author) (2024) A novel Z-scheme SnS/NiAl-LDH/g-C<sub>3</sub>N<sub>4</sub> heterojunction for piezo-photocatalytic degradation of tetracycline: Performance and mechanism. *Surfaces and Interfaces*, 52. 104861. ISSN: 2468-0230

<https://doi.org/10.1016/j.surfin.2024.104861>

---

© 2024 Elsevier. This is an author produced version of an article accepted for publication in *Surfaces and Interfaces*. Uploaded in accordance with the publisher's self-archiving policy. This manuscript version is made available under the CC-BY-NC-ND 4.0 license <http://creativecommons.org/licenses/by-nc-nd/4.0/>.

**Reuse**

Items deposited in White Rose Research Online are protected by copyright, with all rights reserved unless indicated otherwise. They may be downloaded and/or printed for private study, or other acts as permitted by national copyright laws. The publisher or other rights holders may allow further reproduction and re-use of the full text version. This is indicated by the licence information on the White Rose Research Online record for the item.

**Takedown**

If you consider content in White Rose Research Online to be in breach of UK law, please notify us by emailing [eprints@whiterose.ac.uk](mailto:eprints@whiterose.ac.uk) including the URL of the record and the reason for the withdrawal request.



[eprints@whiterose.ac.uk](mailto:eprints@whiterose.ac.uk)  
<https://eprints.whiterose.ac.uk/>

1 **Manuscript submitted to "Surfaces and Interfaces" as a research paper.**

2  
3  
4 A novel Z-scheme SnS/NiAl-LDH/g-C<sub>3</sub>N<sub>4</sub> heterojunction for piezo-photocatalytic

5 degradation of tetracycline: Performance and mechanism

6  
7  
8  
9  
10 Hao Sun<sup>a</sup>, Martin R. Tillotson<sup>b</sup>, Dawei Wang<sup>c</sup>, and Xu Zhao<sup>a\*</sup>

11 *<sup>a</sup>Institute of Blue and Green Development, Shandong University, 264209 Weihai, China*

12 *<sup>b</sup>water@leeds, School of Civil Engineering, University of Leeds, Leeds LS2 9JT, United*

13 *Kingdom*

14 *<sup>c</sup>Key Laboratory of Integrated Regulation and Resource Development of Shallow Lakes,*

15 *Ministry of Education, College of Environment, Hohai University, Nanjing 210098, P.R.*

16 *China.*

17  
18  
19 \*Corresponding author.

20 E-mail addresses: [xuzhao@sdu.edu.cn](mailto:xuzhao@sdu.edu.cn)

## Abstract

The construction of a heterojunction piezo-photocatalyst is one of the most effective strategies to accelerate charge transfer and improve catalytic performance. A novel ternary heterojunction was synthesized by introducing SnS nanoparticles (NPs) onto the surface of a NiAl-LDH/g-C<sub>3</sub>N<sub>4</sub> (LDH/CN) nanosheets *via* a facile hydrothermal method. The separation and transfer paths of carriers was studied for the piezo-photocatalytic degradation of tetracycline (TC), a common antibiotic, under ultrasonic and visible light irradiation. The SnS/LDH/CN piezo-photocatalyst generated a built-in electric field by the piezoelectric effect, which was beneficial for the separation of electron-hole pairs. Furthermore, the Z-scheme heterojunction endowed with a larger surface area, abundant active sites, and improved light-harvesting capacity further improved piezo-photocatalytic performance for TC. In particular, a CLS-30 (30 wt% of SnS on LDH/CN) heterojunction exhibited the highest degradation efficiency with 98.5% removal of TC (20 mg/L) in 60 min, which was higher than that of ultrasonic vibration (38.2%) and visible light illumination (79.4%). TC degradation efficiency remained at almost 90% after 4 consecutive cycles. This work provides a novel viewpoint for designing high-performance and stable heterojunction piezo-photocatalysts for energy limited wastewater remediation applications.

Keywords: SnS/LDH/CN; Tetracycline; Piezo-photocatalysis; Z-scheme heterojunction

## 1. Introduction

44 In recent years the global effort towards net zero carbon emissions and  
45 environmental sustainability goals whilst remediating waterborne pollution has motivated  
46 researchers in wastewater treatment[1-3]. Antibiotics and other pharmaceutical agents,  
47 have been widely used to treat human and animal diseases [4-5], however their excessive  
48 use has resulted in serious human health and ecosystem threats which urgently require  
49 efficient governance strategies, including removal from water [6-8]. Therefore, the  
50 development of environmentally friendly advanced/nano materials, which may utilize  
51 natural energy sources such as sunlight, wind power and acoustic wave, to effectively  
52 treat waterborne pollution is one important element in this effort[9-12]. Photocatalytic  
53 technology is considered an efficient and valuable method for such pollutant degradation  
54 due to its high selectivity, low energy consumption and cyclability [13-15]. In particular,  
55 semiconductor photocatalysts have exhibited remarkable performance in the degradation  
56 of tetracycline (TC), a common class of antibiotic, through the harvesting of solar energy  
57 to convert photons into electron-hole pairs[16-17]. Indeed, a variety of photocatalysts  
58 have been reported for the treatment of waterborne pollutants, including  $\text{TiO}_2$ ,  $\text{g-C}_3\text{N}_4$ ,  
59  $\text{SiO}_2$ ,  $\text{ZnO}$ , and  $\text{CeO}_2$ [18-21]. Graphitic carbon nitride ( $\text{g-C}_3\text{N}_4$ ; CN), with a two-  
60 dimensional layered structure, is the most extensively studied photocatalyst due to its low  
61 band gap, low toxicity, facile preparation and robust chemical stability. In addition, CN

exhibits excellent adsorption capacity, which is also regarded as an attractive property in environmental remediation[22-25]. Nevertheless, the practical applications of a single photocatalyst are restricted because of drawbacks such as low efficiency, insufficient light harvesting ability, and rapid charge-carrier recombination[26-27]. In order to enhance photocatalytic performance and efficiency, various strategies including heterojunction construction, noble metal deposition, and surface morphology modification have been proposed[28-30].

Layered double hydroxides (LDHs) are a class of layered composites with exchangeable anions. They have attracted significant attention in photocatalysis owing to their flexible and tunable chemical composition, intense adsorption capacity, and high chemical stability[31-32]. The coupling of electronegative LDHs with electropositive CN can further enhance the photocatalytic activity of these composites because of synergistic effects induced by the heterointerface under visible light illumination[33-34]. For example, Shakeel *et al.* developed a novel LDH/CN hetero-structured photocatalyst, which showed excellent Rhodamine B degradation performance compared to pure CN or LDH, and was mainly attributed to its large surface area, good conductivity and improved interfacial contact[35]. Moreover, Liu *et al.* reported ZnCr-LDH/CN composite photocatalysts that could significantly improve catalytic water dissociation activity[36].

80 Despite the LDH/CN heterojunction displaying improved photocatalytic efficiency, some  
81 issues such as relatively slow charge transport and poor surface redox properties remained.  
82 For the issue of rapid carriers recombination, most work has focused on material  
83 modification in the realm of photocatalysis, resulting in a single field of research[37-38].  
84 Designing new combinations such as semiconductor heterojunction/piezoelectric  
85 materials might be expected to overcome the limitations of the photocatalytic system and  
86 accelerate the separation of photoinduced charge, thereby improving the catalytic  
87 performance.

88 Polarized electric fields generated by piezoelectric materials under mechanical  
89 energy can promote the separation and transfer of charge carriers. Moreover, charge  
90 separation can enable participation in redox reactions which enhance catalytic activity  
91 and degrade pollutants in water[39-40]. The combination of piezocatalysis and  
92 photocatalysis is regarded as a novel approach for gathering and utilizing abundant  
93 natural energy sources[41-42]. For the past few years, tin sulfide (SnS) has been known  
94 to possess excellent piezoelectric properties and has been application in the piezoelectric  
95 catalysis field. For example, Tian *et al.* reported that SnS nanobelt piezocatalysts  
96 converted CO<sub>2</sub> into acetate with 100% selectivity under the vibration energy[43]. Cao *et*  
97 *al.* prepared a SnS<sub>2</sub>/SnS heterojunction with improved output efficiency by the

piezoelectric effect[44]. Here, the synergistic effect of the SnS piezocatalyst and the LDH/CN heterojunction provided a stable charge supply and accelerated interfacial charge transfer through a built-in electric field. In addition, the redox ability of SnS/LDH/CN composites were further enhanced, which made it one of the most promising piezo-photocatalysts for antibiotic degradation. Although research in environmental remediation has focused on LDH/CN-based photocatalysts there are, to the best of our knowledge, no reports of the Z-scheme SnS/LDH/CN ternary heterojunction as piezo-photocatalysts for degradation of antibiotics.

In this study, we wish to report a novel Z-scheme SnS/LDH/CN heterojunction piezo-photocatalyst prepared via a simple hydrothermal method, and used for high-efficiency degradation of antibiotics. The integration of LDH/CN nanosheets and SnS piezoelectric material combines the advantages of piezoelectric and heterojunction systems which makes it one of the most promising available piezo-photocatalysts for antibiotic degradation. The morphology, surface chemical composition, and piezo-photocatalytic performance of the synthesized SnS/LDH/CN composite were analyzed through a series of characterization and degradation experiments. Furthermore, the mechanism of antibiotic degradation was explored using the results of active species trapping and electron spin resonance (ESR) tests. The work therefore offers a new insight

into the synthesis of ternary heterojunction materials as high-performance piezo-photocatalysts for the degradation of antibiotics.

## 2. Experimental section

### 2.1 Materials

Analytical grade chemicals, including melamine, nickel (II) nitrate hexahydrate ( $\text{Ni}(\text{NO}_3)_2 \cdot 6\text{H}_2\text{O}$ ), aluminum nitrate nonahydrate ( $\text{Al}(\text{NO}_3)_3 \cdot 9\text{H}_2\text{O}$ ), sodium hydroxide ( $\text{NaOH}$ ), sodium carbonate ( $\text{Na}_2\text{CO}_3$ ), polyvinylpyrrolidone (PVP), tin (II) chloride ( $\text{SnCl}_2$ ), thioacetamide, ethanol, and tetracycline (TC) were obtained from Sigma-Aldrich. TC, 1,4-benzoquinone (BQ), tert-butyl alcohol (t-BuOH), ethylenediaminetetraacetic acid (EDTA) and dimethyl sulfoxide ( $\text{C}_2\text{H}_6\text{OS}$ , DMSO) were purchased from the Shanghai Aladdin Biochemical Technology Co., LTD. Deionized (DI) water was used throughout.

### 2.2. Preparation of materials

#### 2.2.1 Preparation of the LDH/CN heterojunction

The LDH/CN composites were fabricated via a simple hydrothermal route. An amount of CN nanosheets were formed by heating melamine in a tube furnace, as reported in previous work[45]. The prepared CN powder was dispersed into 250 mL of deionized water. Following addition of 0.12 M  $\text{Ni}(\text{NO}_3)_2 \cdot 6\text{H}_2\text{O}$  and 0.04 M  $\text{Al}(\text{NO}_3)_3 \cdot 9\text{H}_2\text{O}$ , the



resulting mixture was stirred using a magnetic stirrer bar for 10 min. Subsequently, 0.5 M NaOH and 2.0 M Na<sub>2</sub>CO<sub>3</sub> were dissolved into the above suspension. The pH value of the mixture remained at 9.0, with continuous stirring for 30 min. The resulting homogeneous solution was transferred to a Teflon-lined autoclave which was maintained at 160 °C for 5 h. Finally, the resulting precipitate was recovered and washed, before air-drying at 80 °C overnight. LDH was synthesized without the addition of CN using a similar procedure.

#### *2.2.2 Preparation of SnS/LDH/CN*

In this process, a calculated amount of LDH/CN was placed in 200 mL of deionized water. SnCl<sub>2</sub> (5 mmol) and thioacetamide (5 mmol) were dispersed into the above-mentioned suspension and stirred for 10 min. Then, 200 mg of PVP was added under vigorous stirring. The final suspension was transferred to an autoclave and maintained at 120 °C for 12 h. Deionized water and ethanol were used to wash the product several times. A series of SnS/LDH/CN samples with varying SnS content were prepared, and denoted CLS-10, CLS-20, CLS-30 and CLS-40. SnS was prepared in the absence of LDH/CN using the same method.

#### *2.3 Catalyst characterization*

X-ray diffraction patterns (XRD, D2 PHASER, Bruker) was employed to analyze

crystal structure with Cu K $\alpha$  as radiation source (30 kV,  $\lambda = 1.542 \text{ \AA}$ ) in the  $2\theta$  range of 10–70°. Fourier transform infrared (FTIR) spectra was measured on a Bruker infrared spectrometer (VERTEX 80V, Germany). The surface morphology of the samples were observed using scanning electron microscopy (SEM; S-4300SE, 15 kV) and transmission electron microscopy (TEM; JEM-2100F, JEOL Ltd). X-ray photoelectron spectroscopy (XPS) was carried out on an ESCA LAB MK-II spectrometer with monochromatized Al K $\alpha$  radiation using an ion source energy for charge compensation. The light absorbing potential and band structure were obtained by ultraviolet-visible diffuse reflectance spectra (UV–vis DRS; Hitachi S-3100 spectrophotometer). The specific surface areas (SBET) were measured using a BEL BELSORP device using samples prepared by degassing in vacuum for 12 h. Photoluminescence (PL) spectra were recorded on a RAM Boss analytical instrument to assess charge carrier separation of samples. Electrochemical impedance spectroscopy (EIS) of as-prepared samples was measured by an Ivium electrochemical workstation in a conventional three-electrode system with 0.5 M Na<sub>2</sub>SO<sub>4</sub> solution as the supporting electrolyte. A platinum wire, modified Ni foam, and the Ag/AgCl electrode were employed as the counter, working, and reference electrodes, respectively. The frequency range of measurement was between 0.1 and 10 kHz with a 5 mV amplitude sine-wave potential. The active species in the degradation process were

detected by trapping experiments; 1,4-benzoquinone (BQ), isopropanol (IPA) and ethylenediaminetetraacetic acid (EDTA) were used as scavenging agents for superoxide radical ( $\cdot\text{O}_2^-$ ), hydroxyl radical ( $\cdot\text{OH}$ ) and hole ( $\text{h}^+$ ) species, respectively. Furthermore, electron spin resonance (ESR) measurements were performed on a Bruker EMX PLUS spectrometer using 5,5-dimethyl-1-pyrroline-N-oxide (DMPO) as scavenger.

#### *2.4 Evaluation of degradation efficiency*

The performance of the as-synthesized catalysts was measured by the degradation of TC. Typically, 20 mg catalyst samples were mixed with 100 mL aqueous TC solution (20 mg/L) and stirred continuously for 30 min in the dark to achieve an adsorption/desorption equilibrium. The degradation experiment was then performed under ultrasonic vibration (120 W, 40 kHz) and/or light (200 W Xenon lamp,  $\lambda > 420$  nm, 100 mW/cm<sup>2</sup>). At a given time interval, 5.0 mL of reaction solution was extracted and centrifuged to remove the photocatalyst. The characteristic absorption peak of TC at 357 nm was analyzed using a UV-vis spectrophotometer.

### **3. Results and discussion**

#### *3.1. Structure, morphology, and elemental state*

XRD patterns for all as-prepared catalysts are shown in **Fig. 1(a)**. The XRD spectra of the prepared CN nanosheets showed two distinct emission peaks at 27.3° and 13.1°,

corresponding to the (002) and (100) planes and exhibiting the characteristic structure of aromatic systems and typical interlayer packing[46]. The LDH samples displayed the characteristic peaks of hydrotalcite- type compounds, which were well assigned to a typical hexagonal MgAl-LDH (JCPDF 22-0452). Compared with CN, the (002) peak of LDH/CN was weaker and slightly shifted, and was mainly attributed to the formation of heterojunctions. The diffraction peaks at  $26.1^{\circ}$ ,  $27.5^{\circ}$ ,  $30.6^{\circ}$ ,  $31.4^{\circ}$  and  $39.1^{\circ}$  accord with the (120), (021), (101), (111), and (131) planes, respectively, demonstrating that SnS nanoparticles were synthesized. The XRD spectra of the SnS/LDH/CN samples showed distinctive diffraction peaks for SnS, LDH, and CN; increasing the SnS content of the samples resulted in the LDH and CN diffraction peaks becoming weaker, reflecting the successful combination of SnS and LDH/CN.

The FT-IR spectra were analyzed to further determine the structure of the as-prepared SnS/LDH/CN catalyst (**Fig. 1(b)**). The signals at  $3445\text{ cm}^{-1}$  and  $1350\text{ cm}^{-1}$  were assigned to O-H and  $\text{CO}_3^{2-}$  of LDH stretching vibrations, respectively[47]. In addition, the peak at  $790\text{ cm}^{-1}$  could correspond to the stretching and bending vibrations of metal-oxygen (Al-O, Mg-O) bonds. For the bare SnS sample, the absorption peak at  $570\text{ cm}^{-1}$  was attributed to the Sn-S bond. The bending vibrations of water molecules may account for another peak at  $1637\text{ cm}^{-1}$ . The SnS/LDH/CN composites with different SnS content

showed similar peaks corresponding to the main peaks of SnS, LDH and CN. The FTIR spectra results further demonstrated the successful combination of SnS and LDH/CN, in agreement with XRD data.

The morphologies and microstructures of the as-synthesized samples were analyzed by SEM and TEM, and the resulting images are shown in **Fig. 2**. The pristine CN (**Fig. 2** (a)) revealed an ultrathin lamellar stacked structure. The SEM image of LDH in **Fig. 2** (b) exhibited a layered structure consisting of several thin sheets. The SEM and TEM images (**Fig. 2** (c) and (e)) showed that SnS are spherical nanometer microspheres with particle size. From the SEM and TEM images of the CSL-30 composite (**Fig. 2** (d) and (f)), it may be observed that the SnS NPs and LDH/CN nanosheets were integrated. In agreement with the EDX spectra (**Fig. 2** (k)), the corresponding elemental mappings of SLC-15 (**Fig. 2** (g-l)) clearly demonstrate the presence of C, N, Sn, S, Mg, Al, and Sn, further demonstrating the combination of SnS and LDH in the composites.

**Fig. 3** shows the N<sub>2</sub> adsorption-desorption isotherms and pore size distribution curves for the LDH, LDH/CN, and CLS-30 samples. As displayed in **Fig. 3** (a), the isotherms with type H3 hysteresis loops belong to type IV, which demonstrated the mesoporous structure of the samples. As shown in **Table S1**, the S<sub>BET</sub> of the LDH sample was calculated as 28.27 m<sup>2</sup>/g, providing abundant active sites and high specific surface.

The surface area of LDH/CN and CLS-30 increased significantly with CN and SnS loading, which may be ascribed to the formation of new hybridization. The higher specific surface areas of the heterojunctions are capable of improving the catalytic performance by speeding up charge transfer[48]. The results of pore size distribution are shown in **Fig. 3 (b)**. According to the IUPAC definition, pore sizes in the range 2 nm to 40 nm range for all samples revealed that the pores were mesoporous. Therefore, the prepared samples can effectively adsorb pollutants in the degradation process and enhance catalytic properties.

XPS analysis was used to measure surface chemical compositions and states of the as-prepared catalysts. **Fig. 4 (a)** shows full-scan survey spectra of SnS, LDH, CN and CLS-30. The XPS spectrum for the CLS-30 nanohybrids displays the presence of Sn, S, C, N, Mg, and Al elements. As shown in **Fig. 4 (b)**, the C 1s peak of CN is located at 283.9 eV, and the peak at 287.3 eV may be attributed to graphitic carbon (C-C), and sp<sup>2</sup>-hybridized carbon atoms bonded to N in aromatic rings (N-C=N), respectively. The peak signals of C 1s shifted to a higher binding energy after introducing of SnS and LDH. For LDH nanosheets (**Fig. 4 (c)**), the Ni 2p<sub>3/2</sub> (855.8 eV) and Ni 2p<sub>1/2</sub> (873.4 eV) peaks, along with two satellite peaks, demonstrate the presence of Ni<sup>2+</sup> species. The binding energies of Ni 2p show no obvious change compared with the SnS/LDH/CN heterojunction. As

shown in **Fig. 4** (d), the Al 2p peaks located at 67.9 and 73.2 eV were observed, corresponding to Al 2p<sub>3/2</sub> and Al 2p<sub>1/2</sub>, respectively. For the Sn 3d XPS spectrum (**Fig. 4** (e)), the binding energies at 485.3 eV and 493.8 eV were consistent with the Sn 3d<sub>5/2</sub> and Sn 3d<sub>3/2</sub> states, respectively. The peak intensities of the CLS-30 samples were slightly higher after integrating with LDH/CN. Similarly, the binding energy of S2p (**Fig. 4** (f)) at 161.1 and 162.8 eV may be assigned to S 2p<sub>3/2</sub> and S 2p<sub>1/2</sub>, respectively. The signal peaks of the CLS-15 sample shifted to higher binding energies compared to the bare SnS catalyst, which indicated the decrease of S electron density. Generally, electron density could be changed in binding energies *via* electron screening effects. These findings show that coupling SnS NPs with LDH/CN nanosheets could speed up charge transfer and change the binding energies.

### 3.2. Optical and electronic characteristics

The UV–vis DRS of all the prepared samples are shown in **Fig. 5** (a). The bare SnS exhibited a high absorption edge over the entire visible light region, reflecting its remarkable capability. The LDH sample showed an obvious absorption range from 220 to 300 nm, which was ascribed to the presence of metal cations in the LDH layer. Compared with bare CN and LDH, an improved absorbency and significant red shift in the visible light region was obtained through the generation of LDH/CN composites,

which could be ascribed to rapid charge separation of the heterojunction. The SnS/LDH/CN composites showed significantly enhanced optical adsorption properties with the increased SnS content, indicating interactions between SnS and LDH/CN in the hybrids. Overall the outcomes indicate that adding SnS nanoparticles to LDH/CN nanosheets could increase the number of photoinduced charge carriers and boost photocatalytic performance. The band gap energies **Fig. 5 (b)** for CN, LDH, SnS and SnS/LDH/CN were 2.71, 2.41, 1.67 and 2.48 eV, which were obtained from the extrapolated intercept on the abscissa.

The transfer and separation efficiency of the charge carriers were analyzed using PL measurements. As displayed in **Fig. 6 (a)**, a strong absorption peak was observed for CN around 460 nm. The emission peak for LDH/CN was lower than that of CN, which was in agreement with the enhanced charge transfer efficiency. The SnS/LDH/CN heterojunctions showed a weaker PL peak compared with the binary catalysts, which was mainly attributed to greater availability of electrons and holes for catalytic reactions. The PL signal peak for SnS/LDH/CN also exhibited an obvious blue shift, indicating that the recombination of photogenerated carriers was inhibited. The lowest PL intensity was obtained for the CLS-30 composites in accord with the photocatalytic activity results. The EIS were further employed to measure the transfer process of photoinduced charge



carriers (**Fig. 6 (b)**). The arc radius of an EIS plot reflects the resistance and efficiency of charge transfer[49]. As expected, the results showed that the arc radius for the CLS-30 heterojunction was smaller than that of the single and binary catalysts, corresponding to its faster carrier migration ability.

### 3.3. Piezo-photocatalytic degradation of TC

The catalytic degradation activity of the as-synthesized samples was evaluated through TC degradation under visible light irradiation, ultrasonic vibration, and both visible light irradiation & ultrasonic vibration (**Fig. 7**). As displayed in **Fig. 7(a)**, all as-prepared catalysts exhibited low piezocatalytic ability for degradation of TC, with SnS displaying the highest TC degradation rate (38.2 %). TC was hardly degraded by CN, LDH, or LDH/CN with vibration alone. Meanwhile, the degradation efficiency of SnS/LDH/CN composites gradually improved with increasing SnS content. These results showed that SnS possesses some piezoelectric performance. The photocatalytic results in **Fig. 7(b)** showed the degradation rates followed the order: SnS/LDH/CN > LDH/CN > SnS > LDH > CN. It was clear that the SnS NPs loading on the surface of the LDH/CN could significantly enhance photocatalytic performance, which was ascribed to the formation of a ternary heterojunction. The CLS-30 heterojunctions showed the highest photocatalytic efficiency for TC degradation after 60 min under illumination. Similarly,

CLS-30 achieved the best degradation rate (98.5%) compared with CN, LDH, SnS and LDH/CN under simultaneous ultrasonic vibration and visible light conditions (**Fig. 7(e)**), indicating the synergistic effect of the heterojunction and piezoelectric properties. The pseudo-first-order reaction kinetics for TC degradation is displayed in **Fig. 7 (b, d, f)**. The high reaction rate constant (K) of SnS/LDH/CN reflected the outstanding degradation rate under piezocatalysis, photocatalysis and piezo-photocatalysis. The results further demonstrated that improved degradation efficiency was due to the combination of the LDH/CN heterojunction and piezoelectric effect of SnS. In addition, the stability and durability of the CLS-30 samples was evaluated by recycling experiments (**Fig. 8 (a)**). The piezo-photocatalytic performance of CLS-30 retained high stability (89.3%) after four consecutive cycles. The XRD and XPS patterns (**Figs. S1 and S2**) of the CLS-30 composites showed no significant changes before and after use, indicating structural stability and reusable properties.

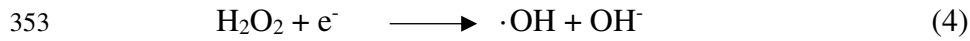
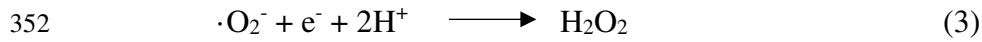
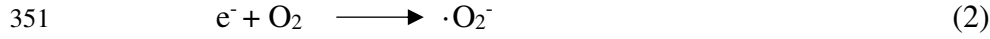
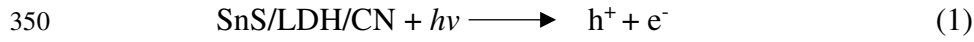
#### *3.4. Mechanistic study*

Trapping tests were carried out using the CLS-30 samples in the presence of various scavengers under identical conditions in order to explore the piezo-photocatalytic degradation mechanism. As shown in **Fig. 8 (b)** EDTA, IPA, and BQ were used as scavenging agents for  $H^+$ ,  $\cdot OH$ , and  $\cdot O_2^-$  species, respectively. The TC degradation

efficiency on the addition of the BQ and EDTA scavengers was suppressed, which demonstrated  $\cdot\text{O}_2^-$  and  $\text{H}^+$  dominated the reaction process. Simultaneously, the introduction of IPA as an  $\cdot\text{OH}$  scavenger showed it played a subordinate role in TC degradation. To further validate the catalytic mechanism, ESR measurements were performed using DMPO as the  $\cdot\text{OH}$  and  $\cdot\text{O}_2^-$  radical scavengers trapping agent. As DMPO- $\cdot\text{OH}$  spectra show (**Fig. 8 (c)**), four characteristic signals (peak intensity = 1:2:2:1) were observed for LDH, LDH/CN and CLS-30, indicating that  $\cdot\text{OH}$  radicals were produced in the three reactions. It is obvious that the  $\cdot\text{OH}$  peak intensity for CLS-30 was stronger than that of pure LDH and binary LDH/CN, which revealed that more  $\cdot\text{OH}$  radicals were generated during the catalytic process. From **Fig. 8 (d)**, six characteristic signals related to  $\cdot\text{O}_2^-$  were exhibited for LDH/CN and CLS-30. However, no obvious characteristic peaks were obtained for LDH, corresponding with the position of its conduction band (CB). Furthermore, CLS-30 showed the strongest DMPO- $\cdot\text{O}_2^-$  signals than those of the other samples, proving that it significantly promoted the formation of  $\cdot\text{O}_2^-$  radicals from molecular oxygen. The results demonstrated that the SnS/LDH/CN heterojunction could effectively enhance the separation efficiency of photogenerated carriers and catalytic performance through the combination of SnS, LDH and CN.

A reasonable mechanism for the SnS/LDH/CN composite in TC degradation was

proposed on the basis of these experimental results (**Fig. 9**). Under light irradiation, the CN, SnS and LDH were excited to produce electron-hole pairs under visible-light irradiation. The photogenerated electrons on the CB of SnS and LDH rapidly migrate and recombine with the holes in the valence band (VB) of CN. Therefore, electrons accumulate in the CB of CN, and the highly positive holes remain in the VB of SnS and LDH, respectively. Here, the Z-scheme heterojunction structure favours the broadening of the carrier transport channel to accelerate charge transfer[50-51]. In the degradation process, the accumulated surface electrons in the CB of CN react with  $O_2$  to generate  $\cdot O_2^-$ , and the photogenerated holes on the VB of SnS and LDH possess sufficient energy to oxidize  $H_2O$  into  $\cdot OH$  radicals. Meanwhile, SnS can generate a built-in electric field under stir, which provides a powerful driving force for the migration and separation of photogenerated carriers. The built-in electric fields can significantly improve degradation efficiency by producing more free radicals and inhibiting recombination of electrons and holes. Therefore, the SnS/LDH/CN composites achieve greater radical density through combination of heterojunction and piezoelectric properties to participate in the degradation of TC, hence showing enhanced piezo-photocatalytic performance. Degradation of TC over the SnS/LDH/CN piezo-photocatalytic system can thus be described:



## 4. Conclusions

We have developed a novel ternary SnS/LDH/CN heterojunction synthesized by a simple hydrothermal method and which exhibits excellent piezo-photocatalytic performance. Notably, the CLS-30 composition catalyst exhibited significantly improved piezo-photocatalytic activity over that of other variants. The improved piezo-photocatalytic performance is attributed mainly to the synergistic effect of both Z-scheme heterojunction and piezoelectric effects for accelerating the transfer of photo-generated carriers. Moreover, the unique nanosheet intercalation structure offers ample active sites and enhances ionic transport electrical conductivity for TC degradation. The prepared SnS/LDH/CN heterojunctions reveal high stability with little activity loss over four continuous cycles. This study therefore offers an innovative method for the synthesis of

highly efficient and Z-scheme heterojunction piezo-photocatalysts for the degradation of TC, which is of significance for environmental remediation.

## **Author contribution statement**

**Hao Sun:** Writing-original draft, Visualization, Validation, Methodology, Investigation, Formal analysis, Writing-review & editing, Data curation, Conceptualization. **Martin R. Tillotson:** Writing-review & editing, Visualization, Investigation. **Dawei, Wang:** Visualization, Investigation. **Xu Zhao:** Writing-review & editing, Visualization, Resources, Funding acquisition.

## **Acknowledgements**

This work was supported by the National Natural Science Foundation of China (No. 72074136, 72033005). And the Taishan Scholar Youth Expert Program of Shandong Province (NO. tsqn202103020).

384

385

386

387

388

389

390

391

392

393

394

395

## 396 **References**

397 [1] S. Khandaker, M.M. Bashar, A. Islam, M.T. Hossain, S.H. Teo, M.R. Awual,

398 Sustainable energy generation from textile biowaste and its challenges: A comprehensive

399 review, *Renew. Sust. Energ. Rev.* 157 (2022) 112051.

400 [2] R. Niu, J. Ren, J.J. Koh, L. Chen, J. Gong, J. Qu, X. Xu, J. Azadmanjiri, J. Min, Bio-

401 Inspired Sandwich-Structured All-Day-Round Solar Evaporator for Synergistic Clean

402 Water and Electricity Generation, *Adv. Energy Mater.* 13 (2023) 2302451.

403 [3] A. Aghahosseini, A.A. Solomon, C. Breyer, T. Pregger, S. Simon, P. Strachan, A.

404 Jäger-Waldau, Energy system transition pathways to meet the global electricity demand

405 for ambitious climate targets and cost competitiveness, *Appl. energy* 331 (2023) 120401.

406 [4] J.R. Rohr, C.B. Barrett, D.J. Civitello, M.E. Craft, B. Delius, G.A. DeLeo, P.J. Hudson,

407 N. Jouanard, K.H. Nguyen, R.S. Ostfeld, J.V. Remais, G. Riveau, S.H. Sokolow, D.

408 Tilman, Emerging human infectious diseases and the links to global food production, *Nat.*

409 *Sustain.* 2 (2019) 445-456.

410 [5] G. Dantas, M.O. Sommer, R.D. Oluwasegun, G.M. Church, Bacteria subsisting on

411 antibiotics, *Science.* 320 (2008) 100-103.

412 [6] M. Diamant, S. Baruch, E. Kassem, K. Muhsen, D. Samet, M. Leshno, U. Obolski,

413 A game theoretic approach reveals that discretizing clinical information can reduce

414 antibiotic misuse, *Nat. Commun.* 12 (2021) 1148.

415 [7] X. Shi, Y. Xa, W. Wei, B.J. Ni, Accelerated spread of antibiotic resistance genes

416 (ARGs) induced by non-antibiotic conditions: roles and mechanisms, *Water Res.* 224

417 (2022) 119060.

418 [8] M.L. Nadimpalli, S.J. Marks, M.C. Montealegre, R.H. Gilman, M.J. Pajuelo, M. Saito,

419 P. Tsukayama, S.M. Njenga, J. Kiiru, J. Swarthout, M.A. Islam, T.R. Julian, A.J. Pickering,



420 Urban informal settlements as hotspots of antimicrobial resistance and the need to curb  
 421 environmental transmission, *Nat. Microbiol.* 5 (2020) 787-795.

422 [9] S. Vyas, P. Prajapati, A.V. Shah, S. Varjani, Municipal solid waste management:  
 423 Dynamics, risk assessment, ecological influence, advancements, constraints and  
 424 perspectives, *Sci. Total Environ.* 814 (2022) 152802.

425 [10] N. Mariotti, M. Bonomo, L. Fagiolari, N. Barbero, C. Gerbaldi, F. Bella, C. Barolo,  
 426 Recent advances in eco-friendly and cost-effective materials towards sustainable dye-  
 427 sensitized solar cells, *Green chem.* 22 (2020) 7168-7218.

428 [11] Y. Lan, Y. Liu, J. Li, D. Chen, G. He, I.P. Parkin, Natural clay-based materials for  
 429 energy storage and conversion applications, *Adv. Sci.* 8 (2021) 2004036.

430 [12] K. Yuan, J. Shi, W. Aftab, M. Qin, A. Usman, F. Zhou, Y. Lv, S. Gao, R. Zou,  
 431 Engineering the thermal conductivity of functional phase-change materials for heat  
 432 energy conversion, storage, and utilization, *Adv. Funct. Mater.* 30 (2020) 1904228.

433 [13] T. Xu, R. Zou, X. Lei, X. Qi, Q. Wu, W. Yao, Q. Xu, New and stable g-C<sub>3</sub>N<sub>4</sub>/HAp  
 434 composites as highly efficient photocatalysts for tetracycline fast degradation, *Appl. Catal.*  
 435 B. 245 (2019) 662-671.

436 [14] Z. Liang, C.F. Yan, S. Rtimi, J. Bandara, Piezoelectric materials for  
 437 catalytic/photocatalytic removal of pollutants: Recent advances and outlook, *Appl. Catal.*

438 B. 241 (2019) 256-269.

439 [15] Y. Lu, Y. Cai, S. Zhang, L. Zhuang, B. Hu, S. Wang, J. Chen, X. Wang, Application  
440 of biochar-based photocatalysts for adsorption-(photo) degradation/reduction of  
441 environmental contaminants: mechanism, challenges and perspective, *Biochar*, 4 (2022)  
442 45.

443 [16] W. Shi, M. Li, X. Huang, H. Ren, F. Guo, Y. Tang, C. Lu, Construction of  
444  $\text{CuBi}_2\text{O}_4/\text{Bi}_2\text{MoO}_6$  p-n heterojunction with nanosheets-on-microrods structure for  
445 improved photocatalytic activity towards broad-spectrum antibiotics degradation, *Chem.*  
446 *Eng. J.* 394 (2020) 125009.

447 [17] X. Yu, J. Huang, J. Zhao, S. Liu, D. Xiang, Y. Tang, J. Li, Q. Guo, X. Ma, J. Zhao,  
448 (Efficient visible light photocatalytic antibiotic elimination performance induced by  
449 nanostructured  $\text{Ag}/\text{AgCl}@ \text{Ti}^{3+}\text{-TiO}_2$  mesocrystals, *Chem. Eng. J.* 403 (2021) 126359.

450 [18] D. Chen, Y. Cheng, N. Zhou, P. Chen, Y. Wang, K. Li, S. Huo, P. Cheng, P. Peng, R.  
451 Zhang, L. Wang, H. Liu, Y. Liu, R. Ruan, Photocatalytic degradation of organic pollutants  
452 using  $\text{TiO}_2$ -based photocatalysts: A review, *J. Clean. Prod.* 268 (2020) 121725.

453 [19] H. Qiu, R. Zhang, Y. Yu, R. Shen, H. Gao,  $\text{BiOI-on-SiO}_2$  microspheres: A floating  
454 photocatalyst for degradation of diesel oil and dye wastewater, *Sci. Total Environ.* 706  
455 (2020) 136043.

- 456 [20] F.H. Abdullah, N.A. Bakar, M.A. Bakar, Current advancements on the fabrication,  
457 modification, and industrial application of zinc oxide as photocatalyst in the removal of  
458 organic and inorganic contaminants in aquatic systems, *J. Hazard. Mater.* 424 (2022)  
459 127416.
- 460 [21] F. Dalanta, T.D. Kusworo, Synergistic adsorption and photocatalytic properties of  
461 AC/TiO<sub>2</sub>/CeO<sub>2</sub> composite for phenol and ammonia–nitrogen compound degradations  
462 from petroleum refinery wastewater, *Chem. Eng. J.* 434, (2022).134687.
- 463 [22] M. Aggarwal, S. Basu, N.P. Shetti, M.N. Nadagouda, E.E. Kwon, Y.K. Park, T.M.  
464 Aminabhavi, Photocatalytic carbon dioxide reduction: Exploring the role of ultrathin 2D  
465 graphitic carbon nitride (g-C<sub>3</sub>N<sub>4</sub>), *Chem. Eng. J.* 425 (2021) 131402.
- 466 [23] G. Mamba, A.K. Mishra, Graphitic carbon nitride (g-C<sub>3</sub>N<sub>4</sub>) nanocomposites: a new  
467 and exciting generation of visible light driven photocatalysts for environmental pollution  
468 remediation, *Appl. Catal. B.* 198 (2016) 347-377.
- 469 [24] X. Zhou, P. Wang, M. Li, M. Wu, B. Jin, J. Luo, M. Chen, X. Zhou, Y. Zhang, Zhou,  
470 X. Synergistic effect of phosphorus doping and MoS<sub>2</sub> co-catalysts on g-C<sub>3</sub>N<sub>4</sub>  
471 photocatalysts for enhanced solar water splitting, *J. Mater Sci Technol.* 158 (2023) 171-  
472 179.
- 473 [25] X. Zhou, X. Yu, L. Peng, J. Luo, X. Ning, X. Fan, X. Zhou, X. Zhou. Pd (II)

474 coordination molecule modified g-C<sub>3</sub>N<sub>4</sub> for boosting photocatalytic hydrogen production,  
 475 J. Colloid Interface Sci. 671 (2024) 134-144.

476 [26] J. Niu, J. Albero, P. Atienzar, H. García, Porous Single-Crystal-Based Inorganic  
 477 Semiconductor Photocatalysts for Energy Production and Environmental Remediation:  
 478 Preparation, Modification, and Applications, Adv Funct Mater. 30 (2020) 1908984.

479 [27] J.A. Nasir, A. Munir, N. Ahmad, T.U. Haq, Z. Khan, Z. Rehman, Photocatalytic Z-  
 480 Scheme Overall Water Splitting: Recent Advances in Theory and Experiments, Adv Mater.  
 481 33 (2021) 2105195.

482 [28] J. Feng, J. Bian, L. Bai, S. Xi, Y. Wang, C. Chen, L. Jing, Efficient wide-spectrum  
 483 photocatalytic overall water splitting over ultrathin molecular nickel  
 484 phthalocyanine/BiVO<sub>4</sub> Z-scheme heterojunctions without noble metals, Appl. Catal. B.  
 485 295 (2021) 120260.

486 [29] Y. Chen, Y. Wang, W. Li, Q. Yang, Q. Hou, L. Wei, L. Liu, F. Huang, M. Ju,  
 487 Enhancement of photocatalytic performance with the use of noble-metal-decorated TiO<sub>2</sub>  
 488 nanocrystals as highly active catalysts for aerobic oxidation under visible-light irradiation,  
 489 Appl. Catal. B. 210 (2017) 352-367.

490 [30] M. Farbod, M. Kajbafvala, Surface modification of TiO<sub>2</sub> nanoparticles by magnetic  
 491 ions: Synthesis and application in enhancement of photocatalytic performance, Appl.

492 Catal. B. 219 (2017) 344-352.

493 [31] G. Zhao, J. Zou, X. Chen, J. Yu, F. Jiao, Layered double hydroxides materials for  
 494 photo (electro-) catalytic applications, Chem. Eng. J. 397 (2020) 125407.

495 [32] S. Mallakpour, M. Hatami, C.M. Hussain, Recent innovations in functionalized  
 496 layered double hydroxides: Fabrication, characterization, and industrial applications, Adv  
 497 Colloid Interfac. 283 (2020) 102216.

498 [33] B. Song, Z. Zeng, G. Zeng, J. Gong, R. Xiao, S. Ye, M. Chen, C. Lai, P. Xu, X. Tang,  
 499 Powerful combination of g-C<sub>3</sub>N<sub>4</sub> and LDHs for enhanced photocatalytic performance: a  
 500 review of strategy, synthesis, and applications, Adv Colloid Interfac. 272 (2019) 101999.

501 [34] Y. Yu, D. Chen, W. Xu, J. Fang, J. Sun, Z. Liu, Y. Chen, Y. Liang, Z. Fang,  
 502 Synergistic adsorption-photocatalytic degradation of different antibiotics in seawater by  
 503 a porous g-C<sub>3</sub>N<sub>4</sub>/calcined-LDH and its application in synthetic mariculture wastewater, J  
 504 Hazard Mater. 416 (2021) 126183.

505 [35] M. Shakeel, M. Arif, G. Yasin, B. Li, H.D. Khan, Layered by layered Ni-Mn-LDH/g-  
 506 C<sub>3</sub>N<sub>4</sub> nanohybrid for multi-purpose photo/electrocatalysis: morphology controlled  
 507 strategy for effective charge carriers separation, Appl. Catal. B. 242 (2019) 485-498.

508 [36] X. Liu, J. Liang, X. Song, H. Yang, X. Li, H. Dai, Y. Song, Y. Liu, J. Hu, X. Pan, X.  
 509 OuYang, Z. Liang, Enhanced water dissociation performance of graphitic-C<sub>3</sub>N<sub>4</sub>

510 assembled with ZnCr-layered double hydroxide, Chem. Eng. J. 337 (2018) 560-566.

511 [37] C. Feng, Z.P. Wu, K.W. Ye, J. Huang, H. Zhang, Surface modification of 2D

512 photocatalysts for solar energy conversion, Adv Mater. 34 (2022) 2200180.

513 [38] L. Xiong, J. Tang, Strategies and challenges on selectivity of photocatalytic oxidation

514 of organic substances, Adv. Energy Mater. 11 (2021) 2003216.

515 [39] X. Yan, G. Li, Z. Wang, Z. Yu, K. Wang, Y. Wu, Recent progress on piezoelectric

516 materials for renewable energy conversion, Nano Energy. 77 (2020) 105180.

517 [40] Y. Zhang, W. Jie, P. Chen, W. Liu, J. Hao, Ferroelectric and piezoelectric effects on

518 the optical process in advanced materials and devices, Adv Mater. 30 (2018) 1707007.

519 [41] L. Zhou, S. Dai, S. Xu, Y. She, Y. Li, S. Leveneur, Y. Qin, Piezoelectric effect

520 synergistically enhances the performance of  $\text{Ti}_{32}$ -oxo-cluster/ $\text{BaTiO}_3$ / $\text{CuS}$  pn

521 heterojunction photocatalytic degradation of pollutants, Appl. Catal. B. 291 (2021)

522 120019.

523 [42] K. Das, D. Majhi, Y.P. Bhoi, B.G. Mishra, Combustion synthesis, characterization

524 and photocatalytic application of  $\text{CuS}/\text{Bi}_4\text{Ti}_3\text{O}_{12}$  pn heterojunction materials towards

525 efficient degradation of 2-methyl-4-chlorophenoxyacetic acid herbicide under visible

526 light, Chem. Eng. J. 362 (2019) 588-599.

527 [43] W. Tian, N. Li, D. Chen, Q. Xu, H. Li, C. Yan, J. Lu, Vibration-driven Reduction of

528 CO<sub>2</sub> to Acetate with 100% Selectivity by SnS Nanobelt Piezocatalysts, *Angew Chem.* 135  
 529 (2023) e202306964.

530 [44] V.A. Cao, M. Kim, W. Hu, S. Lee, S. Youn, J. Chang, H.S. Chang, J. Nah, Enhanced  
 531 piezoelectric output performance of the SnS<sub>2</sub>/SnS heterostructure thin-film piezoelectric  
 532 nanogenerator realized by atomic layer deposition, *ACS nano.* 15 (2021) 10428-10436.

533 [45] L. Li, J. Zhang, Q. Zhang, X. Wang, W.L. Dai, Superior sponge-like carbon self-  
 534 doping graphitic carbon nitride nanosheets derived from supramolecular pre-assembly of  
 535 a melamine-cyanuric acid complex for photocatalytic H<sub>2</sub> evolution, *Nanotechnology*, 32  
 536 (2021) 155604.

537 [46] J. Cheng, Z. Hu, K. Lv, X. Wu, Q. Li, Y. Li, X. Li, J. Sun, Drastic promoting the  
 538 visible photoreactivity of layered carbon nitride by polymerization of dicyandiamide at  
 539 high pressure, *Appl. Catal. B.* 232 (2018) 330-339.

540 [47] K.S. Abou-El-Sherbini, I.M. Kenawy, M.A. Hafez, H.R. Lotfy, Z.M. Abdelbary,  
 541 Synthesis of novel CO<sub>3</sub><sup>2-</sup>/Cl<sup>-</sup>-bearing 3(Mg+Zn)/(Al+Fe) layered double hydroxides  
 542 for the removal of anionic hazards, *J Environ Chem Eng.* 3 (2015) 2707-2721.

543 [48] L. Li, D. Ma, Q. Xu, S. Huang, Constructing hierarchical ZnIn<sub>2</sub>S<sub>4</sub>/g-C<sub>3</sub>N<sub>4</sub> S-scheme  
 544 heterojunction for boosted CO<sub>2</sub> photoreduction performance, *Chem. Eng. J.* 437 (2022)  
 545 135153.

[49] J. Li, Y. Ma, Z. Ye, M. Zhou, H. Wang, C. Ma, D. Wang, P. Huo, Y. Yan, Fast electron transfer and enhanced visible light photocatalytic activity using multi-dimensional components of carbon quantum dots@3D daisy-like In<sub>2</sub>S<sub>3</sub>/single-wall carbon nanotubes, Appl. Catal. B. 204 (2017) 224-238.

[50] J. Luo, X. Ning, L. Zhan, X. Zhou, Facile construction of a fascinating Z-scheme AgI/Zn<sub>3</sub>V<sub>2</sub>O<sub>8</sub> photocatalyst for the photocatalytic degradation of tetracycline under visible light irradiation, Sep. Purif. Technol. 255 (2021) 117691.

[51] Y. Lin, Q. Zhang, Y. Li, Y. Liu, K. Xu, J. Huang, X. Zhou, Peng, F. The evolution from a typical type-I CdS/ZnS to type-II and Z-scheme hybrid structure for efficient and stable hydrogen production under visible light, ACS Sustainable Chem. Eng. 8 (2020) 4537-4546.



564

565

566

567

568

569

570

571

572

573 **Fig. 1.** (a) XRD patterns for CN, LDH, SnS, LDH/CN and SnS/LDH/CN hybrids with  
574 different weight ratios; (b) FT-IR spectra for CN, LDH, SnS, LDH/CN and  
575 SnS/LDH/CN hybrids with different weight ratios.

576 **Fig. 2.** (a) FE-SEM of CN nanosheets; (b) FE-SEM of LDH nanosheets; (c) FE-SEM of  
577 SnS nanoparticles; (d) FE-SEM of CLS-30 hybrid; (e) FE-TEM of SnS nanoparticles; (f)  
578 FE-TEM of CLS-30 hybrid; (g)-(l) elemental mappings of CLS-30; and (m) EDX  
579 spectrum of CLS-30.

580 **Fig. 3.** (a) N<sub>2</sub> adsorption-desorption isotherms of the as-prepared samples; and (b) pore  
581 size distributions of the samples.

582 **Fig. 4.** XPS spectra of CN, SnS, LDH and CLS-30 (a) Survey spectra; (b) C 1s; (c) Ni  
583 2p; (d) Al 2p; (e) Sn 3d; and (f) S 2p.

584 **Fig. 5. (a)** UV-vis DRS spectrum of as-prepared samples; (b) band gap energies of as-  
585 prepared samples.

586 **Fig. 6. (a)** PL spectra of as-prepared samples; and (b) EIS of pure LDH, SnS, LDH/CN,  
587 and CLS-30 composites.

588 **Fig 7.** TC degradation experiments for CN, LDH, SnS, LDH/CN and CLS catalysts for  
589 (a) Piezocatalytic, (c) photocatalytic, and (e) piezo-photocatalytic performance; and (b),  
590 (d) and (f) show the corresponding first-order kinetics plots of the different catalysts.

591 **Fig. 8. (a)** Cycling runs of CLS-30; (b) free radical trapping tests of TC degradation by  
592 CLS-30; and (c-d) ESR spectra of LDH, LDH/CN, and CLS-30.

593 **Fig. 9.** Piezo-photocatalytic mechanism of TC degradation by CLS-30.